PCCP

Accepted Manuscript

ROYAL SOCIETY OF CHEMISTRY

www.rsc.org/pccp

Physical Chemistry Chemical Physics
CREATED USING THE RSC LaTeX PCCP ARTICLE TEMPLATE – SEE www.rsc.org/electronicfiles FOR DETAILS
ARTICLE TYPE
www. rsc.org/xxxxxx | XXXXXXXX

Diffusive and Rotational Dynamics of Condensed n-H_2 Confined in MCM-41†

T.R. Prisk,*‡ M.S. Bryan, and P.E. Sokol

Received Xth XXXXXXXXXX 20XX, Accepted Xth XXXXXXXXX 20XX
First published on the web Xth XXXXXXXXXX 200X
DOI: 10.1039/b000000x

In this paper, we report an inelastic neutron scattering study of liquid and solid n-H_2 confined within MCM-41. This is a high surface area, mesoporous silica glass with a narrow pore size distribution centered at 3.5 nm. The scattering data provides information about the diffusive and rotational dynamics of the adsorbed n-H_2 at low temperatures. In the liquid state, the neutron scattering data demonstrates that only a fraction of the adsorbed o-H_2 is mobile on the picosecond time scale. This mobile fraction undergoes liquid-like jump diffusion, and values for the residence time τ and effective mean-squared displacement $\langle u^2 \rangle$ are reported as a function of pore filling. In the solid state, the rotational energy levels of adsorbed H_2 are strongly perturbed from their free quantum rotor behavior in the bulk solid. The underlying orientational potential of the hindered rotors is due to the surface roughness and heterogeneity of the MCM-41 pore walls. This potential is compared to the hindering potential of other porous silicas, such as Vycor. Strong selective adsorption makes the interfacial layer rich in o-H_2, leaving the inner core volume consisting of a depleted mixture of o-H_2 and p-H_2.

1 Introduction

Developing an understanding of the behaviour of molecular hydrogen within restricted geometries is a priority of the scientific community today. The improvement of hydrogen storage technologies is a primary source of interest in the microscopic dynamics of molecular hydrogen within confinement.[1,2] Neutron scattering has been a leading experimental technique in these efforts because it provides a direct spectroscopic probe of the dynamics and local environment of physisorbed hydrogen. For example, inelastic neutron scattering has been used to study molecular hydrogen confined within carbon-based materials[3–9], clathrates[10], hydrides[11–13], metal-organic frameworks[14–19], and zeolites[19–21]. Neutron scattering techniques are capable of probing the atomic-scale structure[22,23], collective excitations[24–26], rotational energy spectrum[27,28], momentum distribution[29–31], and diffusive dynamics[32] of condensed hydrogen, whether it is in a bulk phase or subjected to confinement.

Mesoporous silica glasses present an opportunity to study hydrogen adsorbed to surfaces which are energetically heterogenous and rough on an atomic-scale. Furthermore, one may study the structure and dynamics of a quantum liquid or solid tightly confined within channels only a few nanometers in diameter. The atomic-scale structure of solid deuterium adsorbed within silica mesopores has been investigated by means of neutron diffraction[33,34]. Within Vycor, a sponge-like borosilicate glass having a disordered pore network, the condensed deuterium gas forms an amorphous solid at the interface with the pore walls. Crystalline deuterium, not necessarily having the same structure as the bulk solid, appears only after a critical pore filling where the adsorbed deuterium begins to occupy the core volume of the pores. In this respect, confined solid deuterium resembles other cryogenic solids confined within porous silicas[35–38]. In contrast to Vycor, MCM-41 is a highly ordered mesoporous silica[39]. Its pore network consists of monodisperse, tubular pores arranged in a hexagonal lattice. Despite the differences in pore morphology, similar results are obtained in neutron diffraction studies of solid deuterium and hydrogen adsorbed within MCM-41.

At low temperatures, the distinction between an amorphous solid component and a nano-crystalline component of the adsorbed hydrogen is reinforced by their observed rotational energy spectra. In the bulk crystal, weak and essentially isotropic interactions between neighbouring molecules lead to free quantum rotor behaviour[40]. However, inelastic neutron scattering measurements of the rotational energy spectrum of solid hydrogen confined within porous Vycor and xerogel glass revealed that only hydrogen molecules occupying the inner core volume of the pores exhibit free rotation[41,42]. Within the interfacial region, the rotational motion of hydrogen rotors is hindered and a broad distribution of transition energies are observed. The atomic-scale surface roughness and irregularities of the Vycor substrate prevent the free rotation of hydrogen molecules directly adsorbed to its irregular pore walls.

The presence of two distinguishable components of adsorbed hydrogen is also reflected in the momentum distribu-

tion of adsorbed hydrogen. It has been shown by deep inelastic neutron scattering that the mean kinetic energy $\langle E_K \rangle$ of helium atoms or hydrogen molecules is enhanced when the helium or hydrogen is adsorbed within silica nanopores[31,42–46]. This increase in kinetic energy $\langle E_K \rangle$ is a quantum-mechanical effect stemming from the uncertainty principle: the atoms/molecules adsorbed to the walls are localized by the attractive forces of the substrate and therefore exhibit a larger zero-point motion than their bulk counter-parts. A measure of local mobility, the mean-squared displacement $\langle u^2 \rangle$ of atoms and molecules is connected to how atoms and molecules are localized by their respective environments. Based on the deep inelastic neutron scattering results, one anticipates that the local mobility $\langle u^2 \rangle$ varies throughout the pore volume, with tightly bound H_2 molecules at the pore walls and more mobile H_2 diffusing within the core volume.

In this paper, we present an inelastic neutron scattering study of the condensed phases of normal hydrogen (n-H_2) confined within MCM-41. The experimental data suggests a picture of condensed n-H_2 confined within small mesporoes in which preferential adsorption plays a significant role. As suggested by previous neutron scattering studies, when the pores are completely saturated, the adsorbed n-H_2 may be conceptually divided into an interfacial layer and the inner core volume. The strong interaction between the adsorbed hydrogen and the mesopore walls determines translational and rotational dynamics within the interfacial layer. H_2 molecules within this layer are tightly bound to adsorption sites, unable to diffuse on short time scales. The surface roughness of the mesopore walls produces a rotational hindering potential which changes their rotational energy levels from free quantum rotor behavior. At the same time, H_2 molecules present within the inner core volume undergo liquid-like jump diffusion, but have much longer residence times than their counter-parts in the bulk liquid phase. Strong selective adsorption makes the interfacial layer rich in o-H_2, leaving the inner core volume consisting of a depleted mixture of ortho-hydrogen and para-hydrogen.

2 Theoretical Background

In this section, we provide a brief introduction to the nuclear spin isomers of molecular hydrogen. In particular, we point out out two salient features of neutron scattering from H_2 for the non-expert reader: how the neutron scattering cross sections for the two nuclear spin isomers differ and how inelastic neutron scattering induces probes the rotational energy spectrum of H_2.

2.1 Spin Isomers of H_2

At low energies where electronic and vibrational degrees of freedom can be neglected, the state vector of free H_2 assumes the form: $|\Psi\rangle = |\psi_T\rangle|J,m\rangle|I,I_z\rangle$, where ψ_T is the translational state of the molecule's centre-of-mass, $|J,m\rangle$ is the rotational state, and $|I,I_z\rangle$ is the nuclear spin state.[40] Because H_2 is a diatomic molecule made up of two identical fermions, its total state vector $|\Psi\rangle$ must be antisymmetric under an exchange or permutation of the two nuclei. Consequently, H_2 molecules in even rotational states must also be in the spin singlet state $I = 0$, while H_2 molecules in one of the odd rotational states must be in one of the spin triplet states $I = 1$. These two different spin isomers of H_2 are known as para-hydrogen (p-H_2) and ortho-hydrogen (o-H_2), respectively.

In bulk gaseous and solid states, the hydrogen molecules are free quantum rotors where the rotational wavefunctions are spherical harmonics and the energy spectrum is given by $E_J = BJ(J+1)$, where $B = 7.35$ meV. In the liquid state, diffusion and interactions between H_2 molecules prevents completely free rotation, and the spherical harmonics are only approximate energy eigenfunctions. Accordingly, the rotational energy spectrum of H_2 within the gas and solid phases consists of sharp transitions between states with different values of J, while these transitions are significantly broadened in the liquid state.

The room temperature equilibrium state of H_2, known as normal hydrogen (n-H_2), has both $J = 0$ and $J = 1$ rotational states fully populated. However states where $J \geq 2$ are sufficiently high in energy that they have negligible population. Thus, since all rotational sublevels are equally populated the ratio of o-H_2 to p-H_2 is approximately 3:1.

At low temperatures, the o-H_2 concentration would be vanishingly small in equilibrium. However, the approach to equilibrium is very slow since the conversion of o-H_2 to p-H_2 requires a change in both the rotational and spin states. This process is doubly forbidden and requires as a fluctuating magnetic field gradient. Consequently, the ortho-to-para conversion is a bimolecular process with a rate constant of a few percent per hour. This allows measurements of n-H_2 to be carried out at low temperatures as long as the measurement time is short compared to the conversion rate.

2.2 Neutron Scattering from H_2

The theory of neutron scattering from homonuclear diatomic molecules in general[47,48] and hydrogen in particular[49,50] has been discussed previously and will be briefly reviewed here.

† Electronic Supplementary Information (ESI) available: [details of any supplementary information available should be included here]. See DOI: 10.1039/b000000x/

Department of Physics, Indiana University, Bloomington, Indiana 47408, USA

‡Current address: Chemical Sciences Division, Oak Ridge National Laboratory, Oak Ridge, Tennessee 37381, USA; E-mail: prisktr@ornl.gov

Considering only low energies, where the molecule remains in its vibrational and electronic ground state, scattering from a H_2 molecule may or may not involve changes in the rotational and nuclear states of the molecule. For elastic scattering, where the rotational state does not change, the strength of the scattering depends dramatically on whether a spin flip can occur. For elastic scattering from p-H_2, spin flips are not possible since it is in the $J = 0, I = 0$ state and the cross section is given by $\sigma_{0\to0} = \sigma_c = 1.76$ barns. Alternately, for o-H_2 spin flip transitions between the $I = 1$ nuclear levels are allowed and the cross section is given by $\sigma_{1\to1} = (3\sigma_c + 2\sigma_i)/3 = 55.3$ barns. Since the elastic scattering from o-H_2 has such a large cross section compared to p-H_2 it will dominate the neutron scattering response in an elastic or quasi-elastic measurement.

Inelastic scattering from H_2 can result in the molecule making transitions between the ortho and para states with the loss or gain of the appropriate rotational energy. In these cases, the nuclear wavefunction will also switch from $I = 0$ to $I = 1$ or vice-versa to maintain the overall antisymmetry of the molecular wavefunction. The appropriate cross sections for these transitions are: $\sigma_{1\to0} = \sigma_i/3 = 26.8$ barns and $\sigma_{0\to1} = \sigma_i = 80.3$ barns. The possible transitions between nuclear spin states are schematically shown in Figure 1.

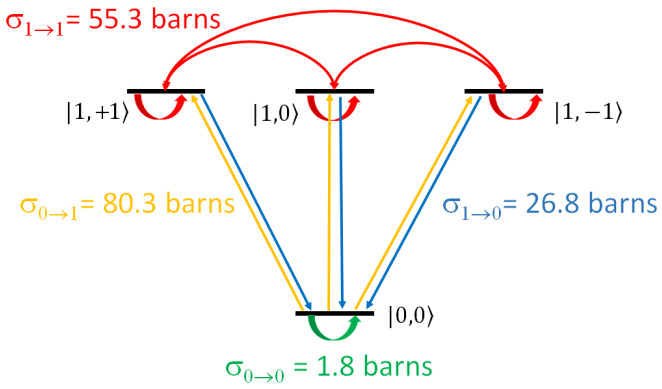

Fig. 1 A scattered neutron may induce a transition in the spin state of an H_2 molecule $|I, I_z\rangle \to |I', I'_z\rangle$. The transitions are marked in coloured arrows: $I = 0 \to I = 0$ in green; $I = 0 \to I = 1$ in yellow; $I = 1 \to I = 0$ in blue; and $I = 1 \to I = 1$ in red. The incoherent scattering cross section for transitions between the $I = 1$ sublevels is sufficiently large to dominate the measured quasi-elastic neutron scattering signal.

3 Experimental Approach

3.1 Sample Characterization

MCM-41 is a highly ordered mesoporous silica glass[39,51,52] produced using a liquid crystal templating technique. The pores of this material are monodisperse, unidirectional, and form a regular hexagonal lattice structure. Our samples were obtained from Sigma-Aldrich[53]. It was characterized using a combination of X-ray powder diffraction and N_2 gas adsorption isotherm measurements. The full details of the sample characterization can be found in the Electronic Supplementary Information of this paper[†]. The X-ray diffraction data establishes the phase purity of the sample and the crystallinity of its pore array. The lattice constant was found to be 4.7 nm. The Brunauer-Emmett-Teller (BET) surface area[54] of the pores is 979 m^2/g The pore size distribution was calculated using the Kruk-Jaroniec-Sayari method[55], and it was found to be a Gaussian centered at 3.5 nm having a full-width at half-maximum of 0.3 nm. The pore walls have a thickness of 1.2 nm. Finally, the total pore volume is 0.92 cc/g.

Using a custom setup, we performed H_2 adsorption isotherm measurements of the MCM-41 sample used in the neutron scattering study. Low temperatures were achieved using a CTI-cyrotronics model 22 refrigerator. An aluminium sample cell which seals by compressing an indium seal was thermally anchored to the cold finger of the displex, and it was loaded with 1.00 g of MCM-41. The temperature of the sample was controlled by means of a PI-loop connected to heaters installed in the displex. Silicon diode thermometers were mounted on the top and bottom of the sample cell in order to verify the absence of significant thermal gradients. Conventional volumetric techniques were employed to dose H_2 gas to the sample cell from an external gas handling system. Corrections for dead volumes were considered.

3.2 Neutron Scattering

A neutron scattering study of condensed n-H_2 confined in MCM-41 was carried out using the Cold Neutron Chopper Spectrometer[56] (CNCS) at the Spallation Neutron Source[57]. This instrument is a direct geometry time-of-flight spectrometer that receives short neutron pulses from a cold coupled moderator. Two incident energies were chosen for this study. First, $E_i = 1.6$ meV ($\lambda = 7.2$ Å) incident neutrons were used to perform a quasi-elastic neutron scattering study of o-H_2 diffusion within MCM-41. Second, $E_i = 20$ meV ($\lambda = 2.0$ Å) incident neutrons were used to probe the rotational energy spectrum of n-H_2 confined in MCM-41. A continuous flow liquid helium cryostat was used to obtain low temperatures. An oscillating radial collimator was used to reduce background scattering from the tail of the cryostat. The detector efficiencies were normalized using a vanadium standard.

The sample cell is a cylindrical aluminium can with an outer diameter of 15.9 mm, a height of 50 mm, and an insert to produce a 1 mm thick annulus. It seals by compressing an indium o-ring, and the top of the cell is shielded by cadmium. The annular space was loaded with a mass of 0.624 g of MCM-41.

The sample was previously outgassed at 120 °C for 24 hr and placed in a sealed container. It was subsequently transferred in open air to the sample cell, which was subsequently degassed by pumping to a pressure $P \leq 10^{-5}$ torr for several hours at room temperature. Gas loading of n-H_2 was performed in situ from an external gas handling system using conventional volumetric techniques. Corrections for the dead volume of the gas manifold, fill line, and sample cell were considered during the gas loading. The temperature was measured by sensors connected directly to the sample cell and the cold finger of the orange cryostat. In addition to measurements of condensed n-H_2 confined in MCM-41, we also performed bulk reference measurements by overfilling the porous material and condensing bulk liquid n-H_2 inside the sample cell.

Steady conversion of o-H_2 to p-H_2 occurs when n-H_2 is cooled to low temperatures. This introduces a time-dependence to the neutron scattering signal. However, our neutron scattering measurements were typically performed for about one hour for each experimental condition after which the cell was rewarmed and hydrogen gas was pumped out of the cell. Conversion of o-H_2 to p-H_2 is negligible during this short measurement time. We verified this by measured for an extended period of time when the pores were fully saturated with liquid.

We performed model fits to our neutron scattering data using the DAVE software package developed by the National Institute of Standards and Technology[58]. Model scattering functions $S(Q,E)$, defined in detail later, were convoluted with instrumental resolution $R(Q,E)$ and fit to the experimentally observed dynamic structure factor $S_{exp}(Q,E)$. The elastic energy resolution for the quasi-elastic neutron scattering measurements $E_i = 1.6$ meV was experimentally determined by measureing the empty MCM-41 matrix at low temperatures. The resolution function was well described by a single Gaussian with a full width at half maximum that increases monotonically from 23 μeV to 31 μeV as Q goes from 0.3 Å^{-}1 to 1.5 Å^{-}1. The elastic energy resolution for higher incident energy studied at $E_i = 20$, also determined by measuring the empty MCM-41 matrix at low temperatures, is approximately 820 μeV and does not have a significant Q-dependence. The inelastic energy resolution was calculated using the Gaussian approximation using time-of-flight monitor data[56].

4 Results

4.1 H_2 adsorption isotherm

The H_2 adsorption isotherm measurements were performed at $T = 19.4 \pm 0.1$ K. Figure 2 plots the specific molar amount of adsorbed H_2 against the relative pressure P/P_0. The adsorption isotherm is Type IV according to the standard IUPAC classification scheme[59]. For the first 20 mmol/g of H_2 gas dosed to the sample, the pores fill by continuous film growth. During the next 7 mmol/g of gas loading, H_2 is adsorbed by means of capillary condensation. Finally, full pore filling is achieved at 31 mmol/g.

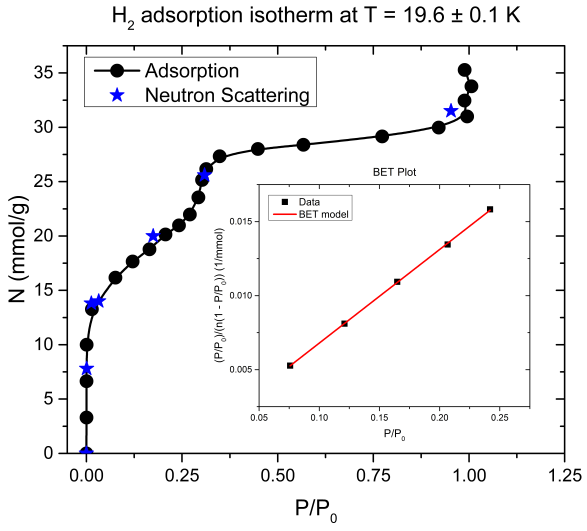

Fig. 2 H_2 adsorption isotherm measurements performed on the MCM-41 sample used in the neutron scattering experiment. The blue stars indicate points where neutron scattering measurements were performed and the observed vapor pressure *in situ*. The inset is a BET plot produced for pressures $0.05 \leq P/P_0 \leq 0.25$ within the film growth regime.

The specific H_2 monolayer capacity can be estimated by performing a BET analysis of the continuous film growth part of the adsorption isotherm[60]. A BET plot using pressures $0.05 \leq P/P_0 \leq 0.25$ for the H_2 adsorption isotherm is shown as an inset to Figure 2. The estimated H_2 monolayer capacity of the MCM-41 sample is 15.7 mmol/g. Assuming the BET surface area obtained from the N_2 isotherm is correct†, the projected surface area of H_2 on MCM-41 is 10.3 Å^2/molecule. The effective molecular cross sectional area σ_m within a hexagonally close packed monolayer is $1.091(M/\rho R)^{2/3}$, where M is the molar mass and ρ is the liquid density. For liquid H_2, $\sigma_m = 14.3$ Å^2/molecule; while for solid H_2, $\sigma_m = 11.7$ Å^2/molecule. Given the fact that the BET theory overestimates monolayer capacity in small pores, as discussed in the supplementary material†, the real cross sectional area σ_m is probably somewhat more than 10.3 Å^2/molecule.

The value of the BET constant C is approximately 126. A value of C greater than 100 for cryogenic adsorption is a sign of a well-defined, localized monolayer[61]. This idea is consistent with our adsorption isotherm measurements and quasi-elastic neutron scattering data. First, the equilibrium vapor

pressure up to 15 mmol/g is close to zero indicating that, at low pore fillings, the H_2 is tightly bound to adsorption sites on the pore walls. Second, as explained below, nearly all of the adsorbed H_2 at 7.8 mmol/g and 13.8 mmol/g pore fillings is non-diffusive on the picosecond time scale. Given the BET constant $C = 126$, the fraction Θ_0 of uncovered surface area when the statistical monolayer coverage is reached is given by $\Theta_0 = 1/(1+\sqrt{C}) = 8.2\%$.

The average density of the adsorbed liquid H_2 at full pore is close to the bulk density. Given the estimated pore volume from the N_2 adsorption isotherm is 0.92 cc/g, the pores would be full of bulk liquid H_2 near 33 mmol/g. This is consistent with full pore being achieved at approximately 31 mmol/g, as observed in the H_2 adsorption isotherm. Presumably, the confined solid has a density which is also close to the bulk solid density. Therefore, full pore for the solid phase is expected to take place around 40 mmol/g.

4.2 Quasi-elastic Broadening

Quasi-elastic neutron scattering measurements of n-H_2 confined in MCM-41 were carried out at a temperature $T = 19.6$ K, which is close to the normal boiling point temperature of the bulk liquid at atmospheric pressure, 20.4 K. The measured pore fillings span a range from sub-monolayer coverage to full pore: $n = 7.8, 13.8, 20.0, 25.6, 31.5$ mmol/g. As noted above, the incoherent scattering cross section of o-H_2 is sufficiently large that the incoherent dynamic structure factor $S_i(Q,E)$ of the o-H_2 completely dominates the experimentally measured signal.

Quasi-elastic neutron scattering measurements were also performed on bulk liquid n-H_2 as a reference by significantly overfilling the MCM-41 sample and condensing over 5 cc of bulk liquid n-H_2 in the sample cell. Very strong quasi-elastic broadening was observed and was fit to a Lorentzian lineshape. For wavevectors 0.3 $\text{Å}^{-1} \leq Q \leq 1.2$ Å^{-1}, the intrinsic full-width at half maximum Γ of the Lorentzian increases monotonically from 0.10 meV to 0.43 meV. No asymptotic value of Γ is approached within this range in Q. These values are in good agreement with previous neutron scattering studies of the bulk liquid[32]. They correspond to hydrodynamic diffusion constants D on the order of 10^{-4} cm^2/sec[62].

A dramatically different picture of the molecular dynamics applies when n-H_2 is confined within nanometre-sized capillary channels. Figure 3 shows selected quasi-elastic neutron scattering data of n-H_2 confined within MCM-41. The experimental scattering data clearly consists of two distinct components. First, there is a resolution-limited elastic peak which corresponds to the presence of adsorbed o-H_2 which is immobile or non-diffusive on the picosecond time scale. Second, the quasi-elastic broadening indicates the existence of an additional fraction of adsorbed o-H_2 which is mobile and diffusive within the experimental time window of CNCS. Up to $Q \leq 1.50$ Å^{-1}, the largest observed width of the quasi-elastic broadening is approximately 200 μeV. The quasi-elastic neutron scattering data presented here demonstrates that confining liquid H_2 within nanometre-scale capillaries results in much slower translational diffusion than takes place within the bulk liquid.

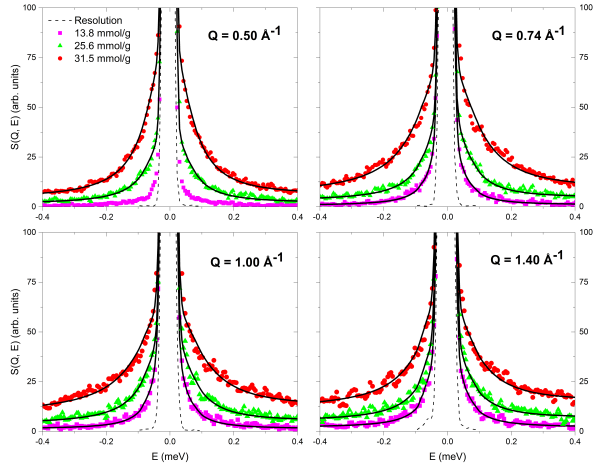

Fig. 3 Representative quasi-elastic neutron scattering data from n-H_2 confined in MCM-41 at $T = 19.6$ K. The background signal from the cryostat, sample cell, and MCM-41 matrix have been subtracted from the data. In order to permit a direct comparison of the quasi-elastic broadening, all of the data has been scaled so that the maximum elastic peak intensity is 1000 arbitrary units. Model fits are shown as solid black curves.

Previous neutron scattering studies of liquid H_2 confined in MCM-41 did not observe any quasi-elastic broadening corresponding to the presence of diffusive hydrogen[60]. Those authors correctly concluded that H_2 molecules adsorbed in MCM-41 are much more translationally confined than their counter-parts in the bulk liquid. They placed an upper limit on the quasi-elastic broadening on the order of 100 μeV. Our neutron scattering measurements are in good agreement with their findings. However, the elastic energy resolution of CNCS for our chosen chopper settings and incident energy is sufficiently fine to observe quasi-elastic broadening produced by slowly diffusing H_2, at least down to a wavevector of $Q = 0.25$ Å^{-1}.

In the hydrodynamic limit $Q \to 0$, the process of continuous diffusion produces Lorentzian broadening in the incoherent dynamic structure factor $S_i(Q,E)$ having a full-width at half maximum of $\Gamma = 2\hbar DQ^2$. At larger values of Q, the neutron spectrometer accesses sufficiently small length scales and sufficiently short time scales to observe elementary dif-

fusion steps and the breakdown of the continuous diffusion picture. The experimentally observed broadening width of n-H_2 confined in MCM-41 is characteristic of liquid-like jump diffusion instead of continuous diffusion. In this diffusive process, molecules occupy quasi-equilibrium sites for a typical residence time τ before making a rapid motion or jump into a new quasi-equilibrium position[63]. Jump diffusion also produces Lorentzian broadening in $S_i(Q,E)$, but, unlike continuous diffusion, Γ approaches an asymptotic value of $2\hbar/\tau$ at high values of Q. For the pore filling $n = 25.6$ mmol/g, the quasi-elastic broadening increases in width for wavevectors up to $Q = 0.5$ Å^{-1}, after which it undergoes little further change with increasing Q. For the highest pore filling studied, $n = 31.5$ mmol/g, the quasi-elastic broadening increases in width with Q for wavevectors up to $Q = 0.8$ Å^{-1}.

The representative quasi-elastic neutron scattering data displayed in Figure 3 shows a strong dependence of the quasi-elastic broadening upon pore filling. At the lowest pore filling measured $n = 7.8$ mmol/g, which corresponds to sub-monolayer coverage, no quasi-elastic broadening was present in the experimental data and only elastic scattering was observed. As the pore filling is increased, the observed width of the quasi-elastic broadening also increases for a fixed value of Q. At partial pore fillings, below $P/P_0 \leq 0.25$, where a thin hydrogen film is adsorbed to the pore walls, the translational motion of the interfacial hydrogen is significantly frustrated by interactions with the pore walls. Close to full pore, $P/P_0 \approx 1$, where the core volume of the pores is also occupied by liquid hydrogen, molecular diffusion is faster, but remains a much slower process than diffusion within the bulk liquid.

4.3 Molecular Spectroscopy

Inelastic neutron scattering measurements of n-H_2 confined in MCM-41 were carried outwithin the liquid phase at $T = 19.6$ K and within the solid phase at $T = 5.8$ K. For the liquid phase study, bulk liquid n-H_2 was measured in addition to pore fillings of $n = 7.8, 13.8, 31.5$ mmol/g. In the solid phase study, three pore fillings were studied $n = 14, 25, 44$ mmol/g, in order to include a monolayer, intermediate, and full pore measurements. The dynamical window of these measurements is sufficient to observe transitions between different rotational energy levels $J \rightarrow J'$.

Colour contour plots of $S(Q,E)$ are shown in Figure 4 for the bulk liquid, the confined liquid, and the confined solid. The background scattering from the sample can and the cryostat have not been subtracted. Positive energy transfers correspond to neutron downscattering, while negative energy transfers correspond to neutron upscattering.

In Figure 4 (a), the dynamic structure factor $S(Q,E)$ of bulk liquid n-H_2 is shown at $T = 19.6$ K. The scattering data consists of several distinct features. First, the elastic line contains the (111), (020), (220), (113), and (222) Bragg reflections of the aluminum sample can at $Q = 2.7, 3.1, 4.4, 5.2$, and 5.4 Å^{-1}, respectively. Second, the recoil spectrum of liquid H_2 extends from the elastic line into positive energy transfers as a broad, concave up band. Third, the rotational transition $J = 0 \rightarrow J = 1$ appears as a dispersionless mode located approximately at +15 meV. Fourth, there is also some weak scattering intensity near -15 meV corresponding to the reverse rotational transition $J = 1 \rightarrow J = 0$. In the bulk solid, H_2 molecules exhibit free quantum rotor behaviour due to the weak and approximately isotropic interactions with their neighbours. However, diffusion and intermolecular interactions produce significant broadening of the $J \rightarrow J'$ transitions in bulk liquid n-H_2, as observed here.

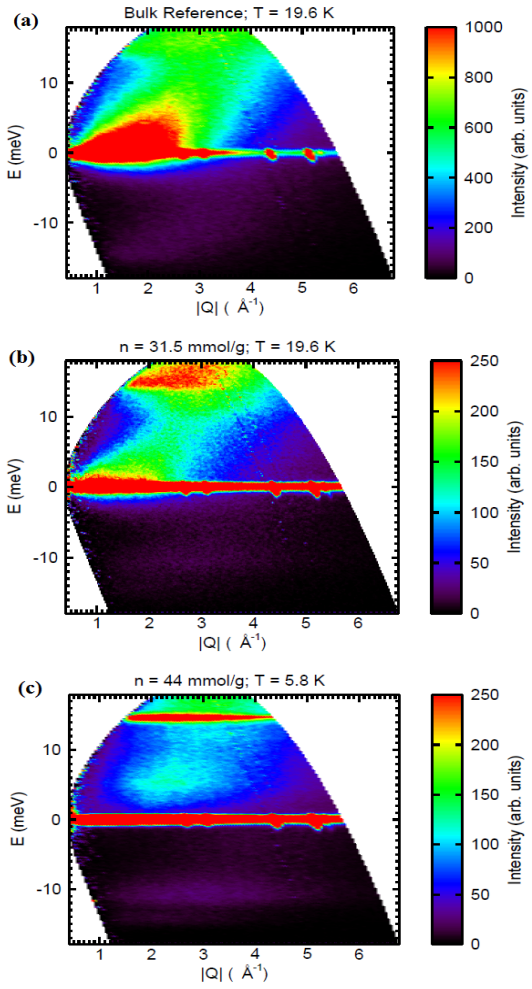

Fig. 4 Colour contour plots of the dynamic structure $S(Q,E)$ of (a) the bulk liquid, (b) confined liquid, and (c) confined solid are compared. The background signal from the cryostat and the MCM-41 matrix has not been subtracted.

In Figure 4 (b), the dynamic structure factor $S(Q,E)$ of the confined liquid at $n = 31.5$ mmol/g pore filling is shown. Like the bulk liquid, one observes the H_2 recoil spectrum emanating from the elastic line and the broad rotational transition $J = 0 \rightarrow J = 1$ located approximately at +15 meV. However, the weak upscattering peak corresponding to the $J = 1 \rightarrow J = 0$ transition is now located at -11 meV. This shift implies that the respective local environments of adsorbed o-H_2 and p-H_2 influence their rotational dynamics in significantly different ways.

In Figure 4 (c), the dynamic structure factor $S(Q,E)$ of the confined solid at $T = 5.8$ K for $n = 44$ mmol/g pore filling is shown. The solidification of the n-H_2 produces no new observable Bragg reflections. The character of the molecular recoil scattering changes in comparison to the confined liquid, suggesting changes in the underlying momentum distribution, final state effects, and rotational form factors. Most importantly, the transitions between rotational energy levels $J \rightarrow J'$ of the confined solid are much sharper than their counter-parts in the confined liquid. In particular, the $J = 0 \rightarrow J = 1$ transition located near +15 meV is much sharper in the solid phase than in the liquid. On the neutron upscattering side, there is a dispersionless mode at -11 meV.

The inelastic scattering function $S(E)$ has been calculated from the dynamic structure factor $S(Q,E)$ by integrating over Q within the range $2.0\ \text{Å}^{-1} \leq Q \leq 5.0\ \text{Å}^{-1}$. The background scattering from the sample cell and the MCM-41 matrix has been removed from $S(E)$.

The inelastic scattering function $S(E)$ of the confined liquid phase at $T = 19.6$ K is shown in Figure 5. Panel (a) plots $S(E)$ for neutron downscattering. Molecular recoil, now essentially averaged over $2.0\ \text{Å}^{-1} \leq Q \leq 5.0\ \text{Å}^{-1}$, produces the continuum scattering between 3 meV $\leq E \leq$ 10 meV. At the two lower pore fillings measured, 7.8 mmol/g and 13.8 mmol/g, an increase in the overall level of scattering begins at +11 meV. As the pore filling is increased toward full pore, there are two peaks within the rotational energy spectrum, located at +11 meV and +15 meV. Both of these peaks are wider than the calculated inelastic energy resolution at those energies. In Figure 5 (b), the contribution of $J = 1 \rightarrow J = 0$ transitions to $S(E)$ are shown. As the pores are filled with liquid, a peak located near -11 meV builds up in intensity on top of a sloping background.

Figure 6 plots the inelastic scattering function $S(E)$ of the confined solid at $T = 5.8$ K as a function of pore filling. In Figure 6 (a), $S(E)$ is shown for positive energy transfers which corresponds to $J = 0 \rightarrow J = 1$ rotational transitions. As in the liquid phase, free molecular recoil produces a smooth continuum up to +10 meV. At 14 mmol/g, close to monolayer coverage, there is a peak at +11 meV. As the pore filling is increased to 25 mmol/g, the peak at +11 meV gains a small amount of intensity and a new, sharp peak appears near +15 meV. When

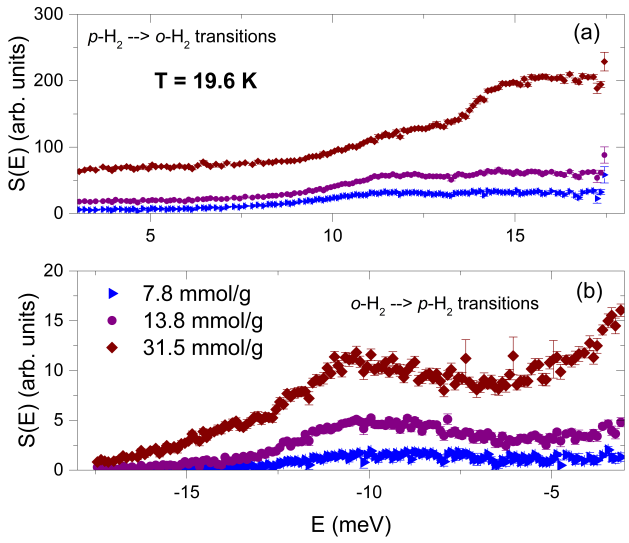

Fig. 5 Energy spectrum $S(E)$ of liquid n-H_2 adsorbed in MCM-41 at 19.6 K. The dynamic structure factor $S(Q,E)$ has been integrated over the range $2.0\ \text{Å}^{-1} \leq Q \leq 5.0\ \text{Å}^{-1}$. The background signal from the cyrostat and the MCM-41 matrix has been subtracted. Positive energy transfers correspond to energy gained by the sample from a scattered neutron.

the pores are full of solid H_2, the peak at +11 meV is no longer observable, and the sharp peak near +15 meV grows in intensity.

Meanwhile, in Figure 6 (b), $S(E)$ is shown for negative energy transfers, thereby corresponding to $J = 1 \rightarrow J = 0$ rotational transitions. At 14 mmol/g, there is a peak located at -11 meV which is more than twice as wide as the energy resolution, which is also shown for comparison. As the pore filling is increased to 25 mmol/g, the broad peak increases in intensity and shifts slightly to lower energies. Finally, at 44 mmol/g, the peak near -11 meV has increased still further in intensity, while a new, resolution-limited peak appears near -14 meV.

5 Discussion

5.1 Diffusive Dynamics

The quasi-elastic neutron scattering data was fit to a model function including three distinct components. First, a narrow Gaussian was used to describe the contribution of elastic scattering to the measured signal. The elastic scattering signal is due to a fraction of adsorbed o-H_2 which is immobile or non-diffusive on the picosecond time scale. Second, a Lorentzian component was used to describe the quasi-elastic broadening. This signal is due to the fraction of adsorbed o-H_2 which is mobile and diffusive within the experimental time window of

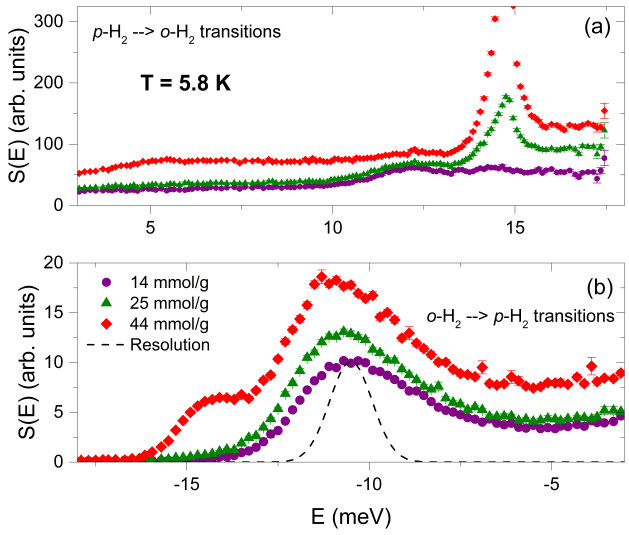

Fig. 6 The rotational energy spectrum of solid n-H_2 adsorbed in MCM-41 at 5.8 K. The dynamic structure factor $S(Q,E)$ has been integrated over the range 2.0 $\text{Å}^{-1} \leq Q \leq 5.0$ Å^{-1}. The background signal from the cyrostat and the MCM-41 matrix has been subtracted. Positive energy transfers correspond to energy gained by the sample from a scattered neutron. Positive energy transfers correspond to energy gained by the sample from a scattered neutron. In panel (a), the full height of the peak located at 14.7 meV for 44 mmol/g gas loading is 516 arbitrary units.

CNCS. Third, a linear background-like component which depends upon the amount of n-H_2 gas loading. Therefore, the incoherent dynamic structure factor $S_i(Q,E)$ is given by the following:

$$S_i(Q,E) = \frac{A_1}{\sqrt{2\pi\sigma_1^2}} e^{-\frac{(E-E_0)^2}{2\sigma_1^2}} + \frac{A_2}{\pi}\frac{\Gamma/2}{(E-E_0)^2+(\Gamma/2)^2} + \alpha E + \beta \quad (1)$$

The free fit parameters include: the integrated area of the Gaussian A_1; the second moment of the Gaussian σ_1^2; the integrated area of the Lorentzian A_2; the full-width at half maximum Γ of the Lorentzian; the common centre E_0 of the Gaussian and Lorentzian; and the slope α and offset β of the linear component. The values of the free parameters are determined by a least-squares fit to the experimental data, including the energy resolution function, which is numerically convoluted with the model function $S_i(Q,E)$.

The Gaussian and Lorentzian components are tied to a common centre located at E_0. Ideally, E_0 would be zero if the energy scale were perfectly defined. However, uncertainties in the moderator emission time or sample attenuation can introduce small shifts in the energy scale. Therefore we treat E_0 as a fitting parameter. Typically, values for E_0 are on the order of 1 μeV which is small compared to the resolution width.

In this model, the elastic scattering is treated as having an intrinsic Gaussian lineshape with a finite width. Strictly, the elastic signal contributes a δ-function peak which has an intrinsic width of 0 μeV. However, we have represented the shape of the elastic signal using a narrow Gaussian, having a typical intrinsic width of 5 μeV. This was done because we found that the fitting routine converged more readily and reliably using the Gaussian representation. Because the measured spectrometer resolution is in the $20-30$ μeV range, it is justified to represent the elastic scattering by a peak with 5 μeV intrinsic width instead of 0 μeV intrinsic width.

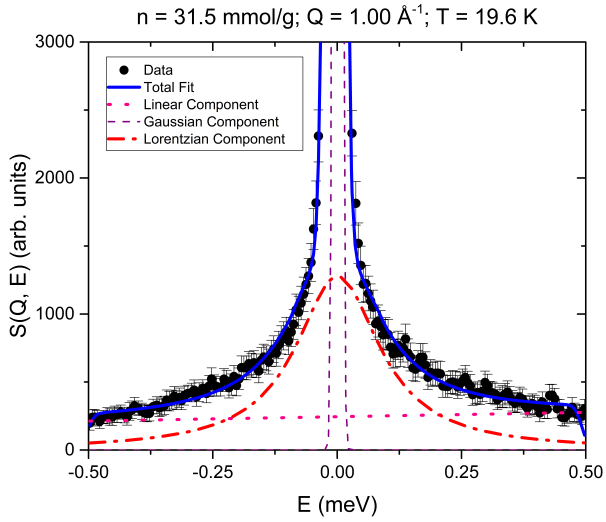

Fig. 7 A representative fit to the quasi-elastic neutron scattering data. The intrinsic lineshapes of each component of the model are shown. The total height of the elastic peak is 22855 arbitrary units.

Figure 7 shows a representative fit to the neutron scattering data at pore filling $n = 31.5$ mmol/g gas loading for wavevector $Q = 1.00$ Å^{-1}. The model function given in Equation 1 provides an excellent fit to the experimental data. Typical values of χ^2 are between 0.3-0.5. Residuals do not reveal any systematic deviations of the model fit from the experimental data. A calculation of the correlation matrix shows that the fit parameters are not strongly correlated with each other. The most significant correlations are those the Lorentzian width Γ and area A_2 have with the offset β of the linear component. Between Γ and β the correlation is -0.73, while it is -0.82 between A_2 and β.

The integrated areas A_1 and A_2 are determined by three factors: the numbers, N_1 and N_2, of o-H_2 molecules in the non-diffusive and diffusive fractions respectively, the rotational

form factor of the H_2 molecule, and an effective Debye-Waller factor[64].

$$A_{1,2} = N_{1,2} j_0^2(Qa) e^{-Q^2\langle u^2_{1,2}\rangle/3} \quad (2)$$

Here j_0 is the zeroth order spherical Bessel function, $a = 0.37$ Åis the radius of gyration of the H_2 molecule, and $\langle u_1^2\rangle$ and $\langle u_2^2\rangle$ are the mean-squared displacements of the molecules within the immobile and mobile components separately. Fitting the Q-dependence of the integrated areas, A_1 and A_2, to Equation 2 permits the extraction of the mean-squared displacement in each component of the adsorbed H_2.

Figure 12 plots the intrinsic linewidth Γ of the Lorentzian component as a function of wavevector Q. As can be seen, the linewidth Γ at a given Q strongly depends upon pore filling. At 7.8 mmol/g, no quasi-elastic broadening is observed. Between 13.8 mmol/g and 31.5 mmol/g, the linewidth Γ at a given value of Q increases monotonically with pore filling. The Q-dependence of the linewidth is consistent with liquid-like jump diffusion since the low Q behaviour is weaker than Q^2 and tends toward an asymptotic value which is equal to $2\hbar/\tau$, where τ is the jump diffusion residence time.

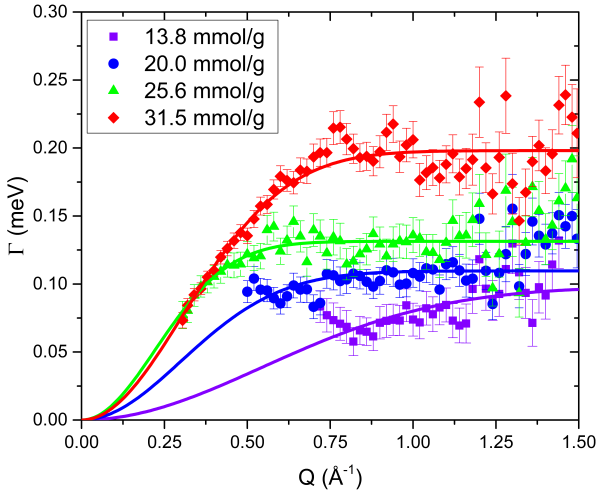

Fig. 8 The intrinsic full-width at half-maximum Γ of the quasi-elastic broadening of n-H_2 confined in MCM-41 at $T = 19.6$ K. The solid lines are fits to the Hall-Ross model which assumes liquid-like jump diffusion having a Gaussian distribution of jump lengths.

In order to obtain the jump diffusion residence time τ, we have fit $\Gamma(Q)$ vs. Q to a number of different models. In Figure 8, the solid lines are fits to the Hall-Ross model[65]. On this theory, jump diffusion takes place between quasi-equilibrium sites where the size of the jumps $\vec{L}$ is stochastically determined. The Hall-Ross model assumes that the probability $P_{\rm HR}$ of a vector displacement $\vec{L}$ has a Gaussian distribution:

$$P_{\rm HR}(\vec{L}) = \frac{1}{(2\pi)^{3/2}} \frac{1}{L_0} e^{-\frac{L^2}{2L_0^2}} \quad (3)$$

The root-mean-square displacement is given by $L_{\rm rms} = \sqrt{\langle L^2\rangle} = L_0\sqrt{3}$. This theory predicts Lorentzian broadening where the linewidth Γ has the following Q-dependence:

$$\Gamma(Q) = \frac{2\hbar}{\tau}\left(1 - e^{-\frac{L^2}{2L_0^2}}\right) \quad (4)$$

As can be seen from Equation 4, as $Q \to \infty$, $\Gamma \to 2\hbar/\tau$. The Gaussian probability distribution $P_{\rm HR}(\vec{L})$ does not correspond to any microscopic calculation and alternative choices for the jump length distribution are also possible. For example, the variable length jump model[66] assumes that $P(L) = \left(L/L_0^2\right)\exp\left(-L/L_0\right)\big)$. This model also predicts a Lorentzian broadening where the asymptotic value of Γ is given by $2\hbar/\tau$. Finally, the residence time τ could also be obtained by fitting only the high Q data to a constant function $\Gamma(Q) = 2\hbar/\tau$. We found that each of these fitting methods produced essentially the same values of the jump diffusion residence time τ.

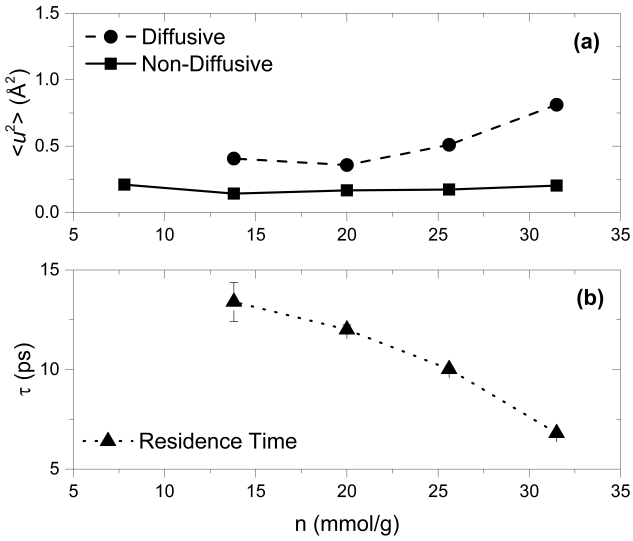

Fig. 9 The model fit parameters of the quasi-elastic neutron scattering data. Where not shown, the error bars are smaller than the symbols. In panel (a), the effective mean-squared displacement $\langle u^2\rangle$ is shown for both the diffusive and non-diffusive fractions of o-H_2 as a function of pore filling. In panel (b), the residence time τ for jump diffusion is shown as a function of pore filling.

The mean-squared displacement $\langle u^2\rangle$ of the non-diffusive and diffusive components was calculated according to Equation 2. Their dependence on pore filling n is shown in Figure 9 (a). As can be seen, the mean-squared displacement $\langle u^2\rangle$ of

the non-diffusive fraction of adsorbed o-H_2 is essentially independent of n. This is because the non-diffusive fraction constitutes the interfacial component of the adsorbed fluid and it is tightly bound to the pore walls. At $n = 13.8$ mmol/g, $\langle u^2 \rangle = 0.14 \pm 0.01$ Å^2, implying that the o-H_2 directly adsorbed to the pore walls are less mobile than H_2 within the bulk solid phase at low temperature where $\langle u^2 \rangle = 0.48 \pm 0.03$ Å^2. This is consistent with deep inelastic neutron scattering studies of H_2 and He confined within porous glasses[42,43,45]. At low temperatures, the mean-squared displacement $\langle u^2 \rangle$ is determined primarily by quantum-mechanical zero-point motion. The localization of H_2 molecules or He atoms by the adsorption potential of the pore walls leads to an enhancement of their average kinetic energy $\langle E_K \rangle$ which is observed in these experiments. Meanwhile, the molecular mobility of the liquid present within the inner core of the mesopores increases as the pores are filled. The effective mean-squared displacement $\langle u^2 \rangle$ increases from 0.41 ± 0.03 Å^2 at 13.8 mmol/g to 0.81 ± 0.01 Å^2 at 31.5 mmol/g. This demonstrates that the o-H_2 occupying the inner core volume is less translationally confined than the o-H_2 which is localized within adsorption sites on the pore walls.

Georgiev *et al* have measured the average kinetic energies $\langle E_K \rangle$ and mean-squared displacements $\langle u^2 \rangle$ of p-H_2 adsorbed to the surface of single-walled carbon nanotubes[5]. A number of their central findings in this system are paralled by H_2 adsorbed to mesoporous silicas. First, they find that the average translational kinetic energy $\langle E_K \rangle$ is essentially temperature independent in physisorbed monolayers. At $T = 17$ K, it decreases from 130 ± 3 K to 83 ± 0.5 K as the surface coverage is increased from 30% to 144% of a monolayer. Second, as noted by those authors, the mean-squared displacements $\langle u^2 \rangle$ increase as the average translational kinetic energy $\langle E_K \rangle$ decreases. It ranges from 0.19 ± 0.03 Å^2 to 0.32 ± 0.10 Å^2. For comparison, it is worth noting the difference in the binding energies of available adsorption sites on carbon nanotubes and MCM-41. On the carbon nanotubes, the isoteric heat of adsorption q_{st} is 75 meV on the groove sites between adjacent nanotubes within a bundle, while the q_{st} is 35 meV on the external surface of the tubes. Edler *et al* report that the surface of MCM-41 is energetically heterogeneous, where q_{st} varies from 35 meV to 18 meV as the surface coverage goes from 20% to 80% of a monolayer[60]. Above a monolayer, q_{st} approaches the heat of liquefaction of bulk H_2, and this is typical for gases adsorbed to heterogeneous surfaces[67].

The residence time τ a function of pore filling n is shown in Figure 9 (b). At 13.8 mmol/g, the jump diffusion residence time is 13.4 ± 1.0 ps and it decreases steadily to 6.80 ± 0.07 ps at 31.5 mmol/g. As the pore filling increases, the diffusive relaxation time decreases, corresponding to faster diffusion. However, even at full pore filling, the residence time τ is much longer than its value in the bulk liquid[63]. Between 15-18 K, the residence time τ within the bulk liquid varies between 2.6-1.1 ps.

In the limit $Q \to 0$, the Hall-Ross model predicts that the Lorentzian linewidth Γ should vary as $\hbar Q^2 L_0^2/\tau$. Therefore, the macroscopic diffusion constant is given by $D = L_0^2/2\tau$. Calculating the diffusion constant for the intermediate 25 mmol/g pore filling yields a value $D = 1.0$ Å^2/ps. At high pore filling, $n = 31.5$ mmol/g, the diffusion constant is $D = 0.8$ Å^2/ps. Both of these diffusion constants are comparable to the diffusion constant[62] of bulk liquid H_2 at 19.6 K, which is 0.9 Å^2/ps. Prima facie, this suggests that macroscopic mass transport of liquid H_2 is not significantly affected by confinement within small mesopores. The longer residence time τ observed in confinement is apparently compensated for by large jump lengths, where the root-mean-square jump length $L_{\rm rms}$ is 7.8 Å and 5.6 Å at 25.6 mmol/g and 37.0 mmol/g, respectively.

However, there are strong reasons to think that a study of molecular diffusion in the continuum or hydrodynamic limit should proceed by means of alternative experimental techniques in this case. First, obtaining the diffusion constant D from the $Q \to 0$ limit of the Hall-Ross model rests upon an extrapolation from the experimental data which is not necessarily justified. A plot of Γ/Q^2 versus Q for our data shows that the hydrodynamic limit is not reached in confined H_2 for wavevectors Q as low as 0.25 Å^{-1}, as shown in Figure 10 (a). Another way of seeing the same point is shown in Figure 10 (b), which plots Γ versus Q^2. A linear fit to the low Q data in Figure 10 (b) yields a finite intercept at approximately 44 μeV. Second, a literal physical interpretation of L_0 would imply much longer jumps in the confined fluid than in the bulk fluid, which is implausible given their comparable density. In the bulk fluid, $L_{\rm rms} \approx 1.1$ Å. Finally, Egelstaff[63] argues that phenomenological pictures of jump diffusion, such as the Hall-Ross model, should be regarded only as illustrative mathematical models which may be used to obtain values for the residence time τ from experimentally measured linewidths Γ. We have used the Hall-Ross model only as a fitting procedure for determining the residence time τ. We conclude that a study of molecular diffusion in the continuum or hydrodynamic limit should probably proceed in this case by means of alternative experimental techniques.

An essentially unchanged value of the translational diffusion constant D of liquid H_2 is not expected on general grounds. The effective kinematic viscosity η of interfacial or confined liquids is typically larger than their bulk counterparts[68,69]. For example, the experimentally measured diffusivity of aqueous solutions through porous silicas is significantly lower than their bulk counterparts. Water within porous silicas forms a relatively immobile and highly viscous layer adjacent to the pore walls[70]. In fact, the local viscosity of flu-

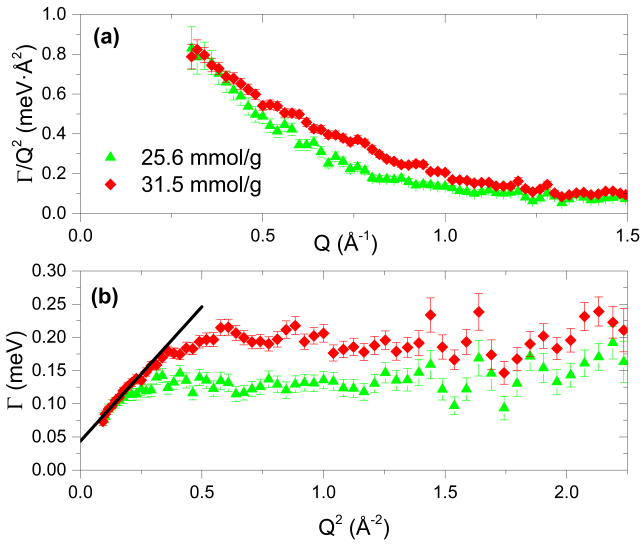

Fig. 10 In the hydrodynamic limit $Q \to 0$, the Lorentzian linewidth Γ varies as Q^2. Here the linewidths for 25.6 mmol/g and 31.5 mmol/g pore filligns are plotted to demonstrate that the $Q-$regime probed here is clearly outside the hydrodynamic limit.

ids within nanometre-scale capillaries may vary in complex ways because of layering and other confinement effects[71–73]. The diffusion constant D of liquid H_2 is related to its kinematic viscosity η by the Stokes-Einstein relation: $D = k_B T/6\pi\eta r$. Given the viscosity at 19.6 K is ≈ 145 μP, the Stokes-Einstein relation is obeyed if H_2 is assumed to have a hydrodynamic radius r of 1.1 Å, which is approximately equal to its van der Waals radius. If the Stokes-Einstein relation remains valid for confined H_2, then an increase in its kinematic viscosity η due to confinement effects should be reflected in a decrease of its microscopic diffusion constant D.

In summary, the quasi-elastic neutron scattering at $T = 19.6$ K demonstrates that the adsorbed o-H_2 makes up two distinct components. First, there is an non-diffusive fraction which contributes the elastic signal to $S(Q,E)$. The mean-squared displacement $\langle u^2 \rangle$ of the immobile fraction is smaller than it is in the bulk crystal and it is independent of pore filling. Second, there is a mobile fraction which undergoes liquid-like jump diffusion. The effective mean-squared displacement $\langle u^2 \rangle$ is larger in the mobile component than in the immobile component. The molecular mobility, as measured by $\langle u^2 \rangle$, increases as the pores are filled with liquid. The jump diffusion residence time τ decreases with increasing pore filling. Altogether, the experimental data suggests a natural interpretation. The adsorbed H_2 can be conceptually divided into an interfacial layer and the inner core volume. The non-diffusive fraction makes up the interfacial layer, so that its constituent H_2 molecules are tightly bound to adsorption sites on the pore walls. At the same time, the diffusive fraction makes up the liquid occupying the inner core volume. In comparison to the bulk fluid, confinement slows the diffusive dynamics of this mobile component down, as shown by the increase of the jump diffusion residence time τ.

5.2 Rotational Dynamics

In this section, we argue that the observed rotational energy spectrum reflects the local environment of adsorbed H_2 and the adsorption potential distinguishes between the two spin isomers of H_2. The selective adsorption of o-H_2 and the rotational hindering potential of the pore walls explains the evolution of $S(E)$ with pore filling, which is shown in Figures 5 and 6. At 14 mmol/g, close to monolayer, all H_2 molecules are directly adsorbed to the pore walls regardless of any preferential adsorption. These adsorbed H_2 molecules directly experience the surface roughness and heterogeneity of the MCM-41 pore walls, which perturbs their rotational wavefunctions and shifts their energy levels from those of a free quantum rotor. At 25 mmol/g, preferential adsorption of o-H_2 distinguishes the behaviour of the two spin isomers. The adsorbed p-H_2 shows both the hindered and free quantum rotor behaviour, while the adsorbed o-H_2 exhibits only hindered rotor behaviour. Presumably, the formation of an o-H_2 rich layer bound to the walls forces p-H_2 to higher adsorbed layers where they can rotate more freely. There is an interfacial layer rich in o-H_2 bound to the pore walls and a depleted mixture of o-H_2 and p-H_2 within the core volume of the pores. The relative temperature-independence of the hindered rotor peak reinforces the fact that the interfacial o-H_2 is non-diffusive and tightly bound to the pore walls.

In the bulk solid, electric quadrupole-quadrupole interactions between nearest neighbours within the crystal primarily determine the intrinsic linewidth of transitions between rotational energy levels[40,74]. The experimentally measured linewidth[32] of the $J = 1 \to J = 0$ quantum rotor transition is 0.75 ± 0.15 meV. For the 25 mmol/g gas loading, we fit the hindered rotor peak to a Gaussian while the free rotor peak was fit to a Lorentzian. The Gaussian peak is located at 11.92 ± 0.04 meV and has an intrinsic width of 1.8 ± 0.1 meV. Meanwhile, the Lorentzian peak is located at 14.69 ± 0.01 meV and has a full width at half maximum of $640 \pm 20\mu$eV. The latter linewidth is the same as the bulk linewidth to within experimental uncertainty. At 44 mmol/g, the Lorentzian peak is located at 14.72 ± 0.02 meV and has an intrinsic width of $440 \pm 10\mu$eV. The latter result is in excellent agreement with previous measurements by Edler *et al*[60], who found a $J = 0 \to J = 1$ peak located at 14.7 ± 0.3 meV having an intrinsic width of $450 \pm 50\mu$eV at high pore fillings. Those authors argued that the confined solid has a local environment close in density and packing to the bulk solid, citing theoret-

ical calculations[74] predicting a linewidth of 580 μeV. Given the disagreement with the measured linewidth within the bulk crystal, this may not be the case. At the same time, neutron diffraction measurements of D_2 confined in MCM-41[34] and Vycor[33] suggest that nearest neighbour distances are not significantly different from their values in the bulk although the structure of the confined crystalline solid seems to be highly distorted. Moreover, our H_2 adsorption isotherm measurements show that the confined liquid fills the pores at approximately bulk liquid density, suggesting that the confined solid is also close to its bulk density.

In the absence of a hindering potential, the rotational energy levels of adsorbed H_2 would correspond to those of a free quantum rotor $E_J = BJ(J+1)$. Transitions between these energy levels would be observed in an inelastic neutron scattering experiment as sharp peaks in $S(E)$. For example, the rotational energy levels of H_2 adsorbed to graphoil, which has a smooth surface on the atomic-scale, are those of a free quantum rotor[75,76]. Porous silica glasses, such as Vycor or MCM-41, have mesopore walls which are rough and heterogeneous on an atomic-scale. H_2 molecules directly adsorbed to the pore walls experience the surface roughness as a hindering potential Vrot which perturbs their rotational wavefunctions and shifts their energy levels away from those of a free quantum rotor. Since the rotational dynamics of the interfacial layer is dominated by interactions with the mesopore walls, the rotational energy spectrum is determined by the distribution of orientational potentials experienced by molecules within the interfacial layer.

White and Lassettre theoretically studied the rotational dynamics of H_2 adsorbed on solid surfaces and the mechanism by which those surfaces discriminate between its spin isomers[77]. They calculated the energy levels of a rigid diatomic rotor moving within a static potential field V produced by the underlying substrate. The interaction potential depends upon the distance z between the centre-of-mass of the adsorbed molecule and the polar angle θ the axis of the diatomic molecule makes with a line normal to the surface. Symmetry requires the static potential V depend only upon z and $\cos^2\theta$. White and Lassettre expanded the potential field V in a Taylor series to lowest order: $V(z,\cos^2\theta) \approx V_a + V_0\cos^2\theta + k(z-z_0)^2$. When only the leading terms in the expansion are considered, the Schrdinger equation is separable into a translational component depending only on z and a rotational component depending only on $\cos^2\theta$.

The rotational hindering potential experienced by an adsorbed H_2 molecule can therefore be approximated by a double well potential of the form $V_{\rm rot} = V_0(1-\cos(2\theta))/2$, where V_0 is the depth of the potential well. The rotational energy levels of H_2 moving within this hindering potential were calculated using the DAVE software[58]. The diatomic rigid rotor calculator numerically solves the Schrdinger equation by diagonalizing the Hamiltonian matrix, which expressed using spherical harmonics $\langle\theta,\phi|J,m\rangle = Y_{Jm}(\theta,\phi)$ as basis functions.

The rotational energy levels E_J of the hindered diatomic rotor are shown in Figure 11 as a function of barrier strength V_0. The rotational ground state energy increases smoothly as the depth of the hindering potential V_0 is increased. The perturbation lifts the degeneracy of the $|1,0\rangle$ and $|1,\pm1\rangle$ states. The transition energy from the ground state to the lowest, degenerate excited state is designated Δ_1, while the transition energy from the ground state to the non-degenerate second excited level is Δ_0. Because there is a one-to-one correspondence between the energy eigenstates of the hindered rotor and those of the free rotor, we still label the perturbed states in terms of J and m, even though these are no longer good quantum numbers.

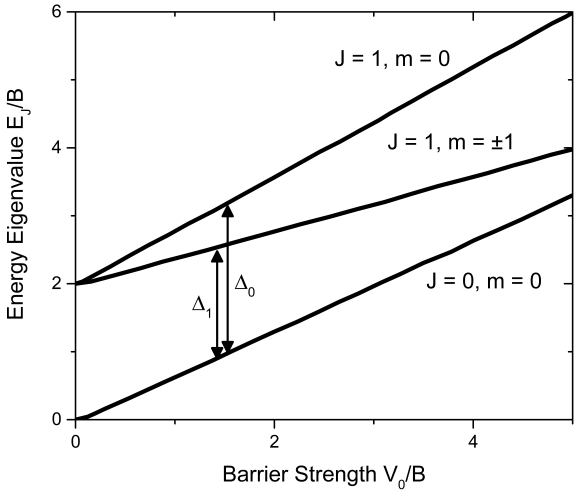

Fig. 11 The perturbed energy levels E_J/B of a hindered quantum-mechanical rotor moving within a double-well potential $V_{\rm rot}(\theta) = V_0(1-\cos(2\theta))/2$ are shown here as a function of the barrier strength V_0/B.

In order to study the rotational hindering potential experienced by adsorbed *o*-H_2 molecules in MCM-41, we performed a lineshape analysis of the broad peak in $S(E)$ near -11 meV. This peak, corresponding to the $J=1\rightarrow J=0$ transition, has a position, width, and shape which is determined by the distribution of potential well depths produced by the MCM-41 mesopore walls. No microscopic calculation or general theory is available to justify a specific choice of model lineshape. As an *ad hoc* model, we have used a skew normal distribution to represent the lineshape of the $J=1\rightarrow J=0$ peak in $S(Q,E)$:

$$S_{1\to0}(E) = \frac{A_3}{\sqrt{2\pi\varepsilon^2}} e^{-\frac{(E-E_p)^2}{2\varepsilon^2}} \left(1 + \mathrm{erf}\left[\frac{\gamma}{\sqrt{2}}\frac{E-E_p}{\varepsilon}\right]\right) + \frac{A_4}{2}\left(1 + \mathrm{erf}\left[\frac{E-E_c}{\sqrt{2\zeta^2}}\right]\right) \quad (5)$$

The Gaussian is determined by its amplitude A_3, second moment ε^2, and location E_p. A finite skewness is added by non-zero values of γ. The second term is used to represent the continuum of inelastic scattering above the $J = 1 \to J = 0$ peak by a smoothed step function. Alternative representations of the continuum scattering, such a polynominal or broad Gaussian, can be used. We found that the fit parameters of the skewed Gaussian were relatively intensitive to how the continuum scattering was represented.

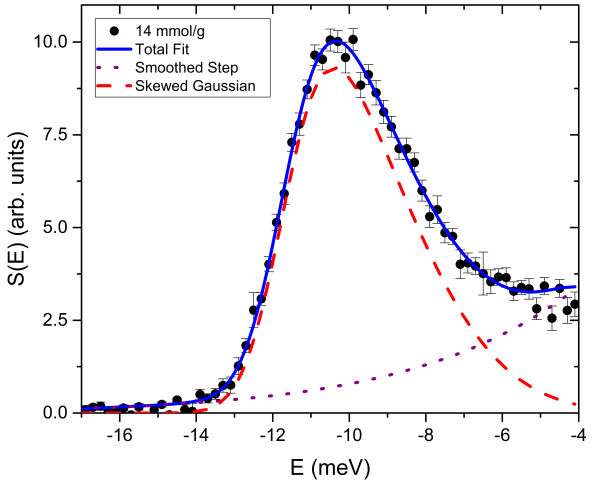

Fig. 12 A least-squares fit to the rotational energy spectrum of n-H_2 at negative energy transfers. The intrinsic lineshapes of each component in the model are shown. The calculated inelastic energy resolution has been folded into the total fit (blue curve). The peak located at -11 meV is described by a skewed Gaussian function.

In Figure 12, a fit to $S(E)$ versus E to Equation 5 is shown for the 14 mmol/g pore filling. The model produces a good fit to the experimental data, where $\chi^2 = 1.2$. Residuals do not reveal any systematic differences between the model fit and the data. The Gaussian peak position is $E_p = -11.7$ meV, which is in agreement with the measurements of Elder *et al*, 11.8 ± 0.2 meV. Because of the skewed shape, the maximum intensity of the entire line is located further to the right at -10.5 meV. A calculation of the correlation matrix shows that each of the free fit parameters of the skew Gaussian are not significantly correlated with other fit parameters in Equation 5. Two of the parameters of the smooth step function, A_4 and E_c, have a correlation coefficient of 0.95. However, we do not ascribe any physical significant to the parameters of the smoothed step function.

As shown in Figure 12, the energy Δ_1 of the $|1,\pm1\rangle \to |0,0\rangle$ rotational transition is -10.5 meV in the solid monolayer. The White-Lassettre model accordingly predicts that the energy Δ_0 of the $|1,0\rangle \to |0,0\rangle$ rotational transition is -16.8 meV. It is clear from Figure 12 that no separate peak corresponding to this transition is present in the neutron energy gain data. This may appear to be inconsistent with the White-Lassettre theory, which predicts a splitting of the $J = 1$ sublevels. However, it should be emphasized that the data shown in Figure 12 is for *negative* energy transfers: the intensity of any observed rotational transitions is proportional to the population of the $J = 1$ sublevels. The energy of the $|1,0\rangle$ state is 6.3 meV (73 K) higher than the $|1,\pm1\rangle$ states, and it is therefore likely that the thermal population of the $|1,0\rangle$ is much smaller than the thermal population of the $|1,0\rangle$ at $T = 5.8$ K.

The White-Lassettre approach can be used to calculate the orientational potential distribution of MCM-41 from our inelastic neutron scattering data. As shown in Figure 12, the Δ_1 of the $|1,\pm1\rangle \to |0,0\rangle$ transition at monolayer coverage can be described by a skewed Gaussian function. If adsorbed H_2 molecules experienced a single, well-defined value of V_0, then in the experimental data there would be a shift in the location of this transition away from 14.7 meV, but no additional broadening beyond instrumental resolution would be observed. The intrinsic shape and width of the peak is determined by a distribution of potential well depths V_0 stemming from the inhomogeneous character of the MCM-41 pore walls. By means of the White-Lassettre model, the energy scale shown in Figure 12 has a one-to-one correspondence with possible values of V_0.

The normalized distribution $P(V_0)$ of potential barriers V_0 of MCM-41 is compared to Vycor[41] in Figure 13. In Vycor, there is a broad, asymmetrical peak located at $V_0/B = 3.5$. In contrast, the orientational potential distribution in MCM-41 forms a relatively narrow, symmetrical peak located at $V_0/B = 2.2$. The observed difference in the orientational potential distribution $P(V_0)$ constitutes clear experimental evidence that the pore walls of MCM-41 are smoother than those in Vycor on an atomic-scale. Both of these materials have smoother pore walls than Britesorb[42], where the shift in the rotational transition energies is even larger. It is important to note that $P(V_0)$ has been calculated for both MCM-41 and Vycor using the White-Lassettre approach. The direct comparison of the resulting curves is justified by the fact that both determinations make the same set of theoretical assumptions.

The translational mobility of adsorbate molecules is reduced by surface roughness, just as the rotational wavefunctions of adsorbed molecules are perturbed by hindering poten-

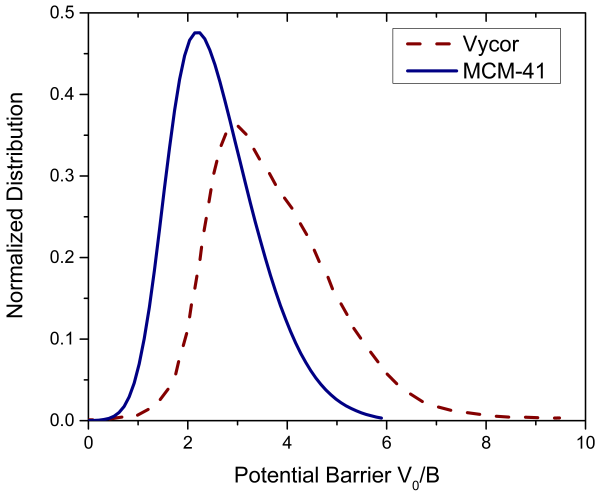

Fig. 13 The normalized potential barrier distribution of the hindered H_2 rotors. The difference between the potential barrier distribution experienced by a monolayer of H_2 adsorbed to MCM-41 and Vycor[41] is explained by differences in heterogeneity and atomic-scale surface roughness of the pore walls.

tial barriers[41]. The atomic-scale irregularities of the substrate increase the effective strength of the local adsorption potential in porous materials with rough internal surfaces. This is demonstrated in pulse-gradient nuclear magnetic resonance studies of ^{3}He diffusion within MCM-41[78,79] and Vycor[80,81]. Close to monolayer coverage at very low temperatures, ^{3}He atoms move between different adsorption sites on the mesopore walls by means of quantum-mechanical tunnelling instead of thermally activated diffusion. Surface roughness determines, in large part, the potential barrier between adsorption sites and therefore the tunnelling rates of adsorbed ^{3}He atoms[82]. The ^{3}He tunnelling rate on the surface of Vycor is $10^5 - 10^6$ s^{-1}, while on the mesopore walls of MCM-41 it is $\approx 10^7$ s^{-1}.

The fact that ^{3}He diffusion is faster in the quantum tunnelling regime adsorbed to MCM-41 than Vycor is consistent with our finding that the rotational motion of H_2 molecules are the pore walls are less perturbed in MCM-41 than in Vycor. Measuring the rotational energy levels of adsorbed molecules may be a useful technique for characterizing the atomic-scale surface roughness of heterogeneous solid surfaces. For example, recently, a detailed model of MCM-41 has been developed which incorporates the surface roughness of the pore walls[83]. In principle, such models could be tested, or at least empirically parameterized, by computing the rotational energy spectrum of adsorbed molecules and comparing the theoretical spectrum to experimental data.

5.3 Selective Adsorption

The interaction of solid substrates with molecular hydrogen strongly distinguishes between its two spin isomers, p-H_2 and o-H_2, leading to preferential adsorption of o-H_2. This phenomenon has been experimentally observed on a number of different materials, such as activated alumina[84,85], porous Vycor glass[41], and amorphous ice[86]. It is due to the anisotropy of the local adsorption potential, which lowers the free energy of bound o-H_2 relative to p-H_2. For example, on amorphous ice the preferential adsorption of o-H_2 and relative depletion of p-H_2 is due to the anisotropy of the of the adsorption potential. The p-H_2 spin isomer is bound only by the spherically symmetric part of the potential while o-H_2 experiences additional binding from the anisotropic part of the potential.

The separation factor S measures the preferential adsorption of o-H_2:

$$S = \frac{(\rho_o/\rho_p)_{\text{ads}}}{(\rho_o/\rho_p)_{\text{bulk}}} \tag{6}$$

The numerator $(\rho_o/\rho_p)_{\text{ads}}$ is the molar ratio of o-H_2 to p-H_2 within the adsorbed phase, while the denominator $(\rho_o/\rho_p)_{\text{bulk}}$ is the same molar ratio within the bulk state. Immediately after condensation from a gas at room temperature (n-H_2), $\rho_o/\rho_p = 3$. The separation factor is defined so that it is always equal to or greater than unity.

At low temperatures, the separation factor S can be estimated using the White-Lassettre model:

$$S = \frac{1}{3}\exp\left(\frac{2B-\Delta_0}{k_BT}\right) + \frac{2}{3}\exp\left(\frac{2B-\Delta_1}{k_BT}\right) \tag{7}$$

The separation factor S depends upon temperature T so that the substrate more strongly selects o-H_2 at lower temperatures T. In the solid state at 14 mmol/g pore filling, the observed transition energy Δ_1 is 10.5 meV and the White-Lassettre model predicts that $\Delta_0 = 16.8$ meV. At 5.8 K, the separation factor S is approximately 1480, implying that the interfacial layer is composed of essentially 100% o-H_2. At 19.6 K, the separation factor S is 4.2. In the liquid state, the interfacial layer is composed of 93% o-H_2.

6 Conclusions

We have studied the translational and rotational dynamics of condensed n-H_2 confined within MCM-41 using neutron scattering. The porous MCM-41 sample used in the neutron scattering experiment was characterized in detail using small-angle X-ray diffraction and N_2 adsorption isotherm measurements[†]. The characterization data confirms that the MCM-41 sample is highly ordered and reveals a narrow pore size distribution centred at 3.5 nm. The neutron scattering data is also coupled to H_2 adsorption isotherm measurements,

which permit the identification of the gas loadings where monolayer coverage and full pore filling are achieved.

The experimental data supports a detailed picture of condensed n-H_2 confined within small, tubular mesopores. At full pore, the adsorbed n-H_2 may be conceptually divided between the interfacial layer and the inner core volume. The translational and rotational dynamics of the interfacial layer are dominated by strong interactions with the mesopore walls. H_2 molecules within the interfacial layer are tightly bound to adsorption sites, and are thereby non-diffusive on the picosecond time scale. They directly experience the surface roughness and heterogeneity of the MCM-41 pore walls in the form of a hindering potential which perturbs their rotational wavefunctions and energy levels. The adsorption potential distinguishes between the spatially symmetric and antisymmetric rotational wavefunctions of p-H_2 and o-H_2, leading to preferential adsorption which makes the interfacial layer rich in o-H_2.

Meanwhile, the behaviour of the H_2 molecules occupying the inner core volume is dominated by confinement effects. They undergo observable liquid-like jump diffusion, but the residence time of the jumps in confinement is much longer than the residence time in the bulk liquid. The rotational energy levels of the molecules within the inner core resembles those of the bulk phases. The inner core consists of a mixture of o-H_2 and p-H_2 which has been somewhat depleted of o-H_2 by the preferential adsorption of the mesopore walls.

7 Acknowledgements

The authors gratefully acknowledge helpful discussions with Georg Ehlers, and Sara Skrabalak for making the Micromeritics ASAP 2020 Physisorption Analyzer available for use in this work. This report was prepared under Award 70NANB5H1163 from the National Institute of Standards and Technology, US Department of Commerce. The statements, findings, conclusions, and recommendations are those of the authors and do not necessarily reflect the views of the National Institute of Standards and Technology or the U.S. Department of Commerce. This research at Oak Ridge National Laboratorys Spallation Neutron Source was sponsored by the Scientific User Facilities Division, Office of Basic Energy Sciences, U.S. Department of Energy.

References

1 D. P. Broom, *Hydrogen Storage Materials*, Springer-Verlag, London, 2011.
2 G. Walker, *Solid-State Hydrogen Storage: Materials and Chemistry*, CRC Press, Boca Raton, FL, 2008.
3 A. J. Horsewill, K. Goh, S. Rols, J. Ollivier, M. R. Johnson, M. H. Levitt, M. Carravetta, S. Mamone, Y. Murata, J. Y. C. Chen, J. A. Johnson, X. Lei and N. J. Turro, *Phil. Trans. R. Soc. A*, 2013, **371**, 20110627.
4 H. G. Schimmel, G. J. Kearley, M. G. Nijkamp, C. T. Visser, K. P. de Jong and F. M. Mulder, *Chemistry A European Journal*, 2003, **9**, 4764–4770.
5 P. A. Georgiev, D. K. Ross, A. De Monte, U. Montaretto-Marullo, R. A. H. Edwards, A. J. Ramirez-Cuesta, M. A. Adams and D. Colognesi, *Carbon*, 2005, **43**, 895 – 906.
6 P. A. Georgiev, D. K. Ross, P. Albers and A. J. Ramirez-Cuesta, *Carbon*, 2006, **44**, 2724 – 2738.
7 C. M. Brown, T. Yildirim, D. A. Neumann, M. J. Heben, T. Gennett, A. C. Dillon, J. L. Alleman and J. E. Fischer, *Chemical Physics Letters*, 2000, **329**, 311 – 316.
8 D. G. Narehood, M. K. Kostov, P. C. Eklund, M. W. Cole and P. E. Sokol, *Phys. Rev. B*, 2002, **65**, 233401.
9 D. G. Narehood, J. V. Pearce, P. C. Eklund, P. E. Sokol, R. E. Lechner, J. Pieper, J. R. D. Copley and J. C. Cook, *Phys. Rev. B*, 2003, **67**, 205409.
10 K. T. Tait, F. Trouw, Y. Zhao, C. M. Brown and R. T. Downs, *J. Chem. Phys.*, 2007, **127**, 134505.
11 Y. Fukai, *The Metal-Hydrogen System*, Springer, Berlin, 2005.
12 S. F. Parker, S. J. C. Jayasooriya, U. A., M. Bortz and K. Yvon, *J Chem Soc Faraday Trans*, 1998, **94**, 25952599.
13 S. F. Parker, S. M. Bennington, A. G. Ramirez-Cuesta, A. J., W. Bronger, H. Herman, K. P. J. Williams and T. Smith, *J Am Chem Soc*, 2003, **125**, 1165611661.
14 H. Furukawa, K. E. Cordova, M. O'Keeffe and O. M. Yaghi, *Science*, 2013, **341**, 1230444.
15 N. L. Rosi, J. Eckert, M. Eddaoudi, D. T. Vodak, J. Kim, M. O'Keeffe and O. M. Yaghi, *Science*, 2003, **300**, 1127–1129.
16 W. L. Queen, E. D. Bloch, C. M. Brown, M. R. Hudson, J. A. Mason, L. J. Murray, A. J. Ramierz-Cuesta, V. K. Peterson and J. R. Long, *Dalton Transcations*, 2012, **41**, 4180–4187.
17 K. Sumida, S. Horike, S. S. Kaye, Z. R. Herm, W. L. Queen, C. M. Brown, F. Grandjean, G. J. Long, A. Dailly and J. R. Long, *Chem. Sci.*, 2010, **1**, 184–191.
18 C. M. Brown, Y. Liu, T. Yildirim, V. K. Peterson and C. J. Kepert, *Nanotechnology*, 2009, **20**, 204025.
19 J. Luo, H. Xu, Y. Liu, Y. Zhao, L. L. Daemen, C. M. Brown, T. V. Timofeeva, S. Ma and H. C. Zhou, *J Am Chem Soc*, 2008, **130**, 9626–9627.
20 F. Nouar, J. Eckert, J. F. Eubank, P. Forster and M. Eddaoudi, *J Am Chem Soc*, 2009, **131**, 2864–2870.
21 J. DeWall, R. M. Dimeo and P. E. Sokol, *J. Low Temp. Phys.*, 2002, **129**, 171–184.
22 A. Cunsolo, G. Pratesi, D. Colognesi, R. Verbeni, M. Sampoli, F. Sette, G. Ruocco, R. Senesi, M. H. Krisch and M. Nardone, *J. Low Temp. Phys.*, 2002, **129**, 117–131.
23 M. Zoppi, U. Bafile, M. Celli, G. J. Cuello, F. Formisano, E. Guarini, R. Magli and M. Neumann, *J. Phys.: Condens. Matter*, 2003, **15**, S107–S112.
24 K. Carneiro, M. Nielsen and J. P. McTague, *Phys. Rev. Lett.*, 1973, **30**, 481.
25 F. J. Bermejo, J. L. Martinez, D. Martín, F. J. Mompean, M. García-Hernández and A. Chahid, *Physics Letters A*, 1991, **158**,.
26 C. Mondelli, M. A. González, F. Albergamo, C. Carbajo, M. J. Torralvo, E. Enciso, F. J. Bermejo, R. Fernández-Perea, C. Cabrillo, V. Leon and M. L. Saboungi, *Phys. Rev. B*, 2006, **73**, 094206.
27 D. Colognesi, *Applied Physics A*, 2002, **74**, S64.
28 J. Z. Larese, T. Arnold, L. Frazier, R. J. Hinde and A. J. Ramierz-Cuesta, *Phys. Rev. Lett.*, 2008, **101**, 165302.
29 F. Fernandez-Alonso, F. J. Bermejo, C. Cabrillo, R. O. Loutfy, V. Leon and M. L. Saboungi, *Phys. Rev. Lett.*, 2008, **98**, 215503.
30 W. Langel, D. L. Price, R. O. Simmons and P. E. Sokol, *Phys. Rev. B*, 1988, **38**, 275–282.
31 R. N. Silver and P. E. Sokol, *Momentum Distributions*, Plenum Press, New York, 1989.

32 P. A. Egelstaff, B. C. Haywood and F. J. Webb, *Proc. Phys. Soc.*, 1967, **90**, 681.
33 Y. Wang, W. M. Snow and P. E. Sokol, *J. Low Temp. Phys.*, 1995, **101**, 929–949.
34 N. Floquet, J. P. Coulomb and G. André, *Microporous and Mesoporous Materials*, 2004, **72**, 143.
35 D. E. Silva, P. E. Sokol and S. N. Ehrlich, *Phys. Rev. Lett.*, 2002, **88**, 155701.
36 P. Huber, D. Wallacher and K. Knorr, *J. Low Temp. Phys.*, 1998, **111**, 419.
37 P. Huber, D. Wallacher and K. Knorr, *Phys. Rev. B*, 1999, **60**, 666.
38 B. S. Shirato, M. P. Fang, P. E. Sokol and S. Komarneni, *Science*, 1995, **20**, 369.
39 X. S. Zhao, G. Q. Lu and G. J. Mullar, *Ind. Eng. Chem. Res.*, 1996, **35**, 2075.
40 I. F. Silvera, *Rev. Mod. Phys.*, 1980, **52**, 393–452.
41 D. W. Brown, P. E. Sokol and S. A. FitzGerald, *Phys. Rev. B*, 1999, **59**, 258–266.
42 D. G. Narehood, N. Grube, R. M. Dimeo, D. W. Brown and P. E. Sokol, *J. Low Temp. Phys.*, 2003, **132**, 223–237.
43 C. Andreani, C. Pantalei and R. Senesi, *Phys. Rev. B*, 2007, **75**, 064515.
44 D. Nemirovsky, R. Moreh, K. H. Andersen and J. Mayers, *J. Phys.: Condens. Matter*, 1999, **11**, 6653.
45 Y. Wang and P. E. Sokol, *J. Low Temp. Phys.*, 1991, **83**, 165.
46 K. H. Herwing, J. L. Gavilino, M. C. Schmidt and R. O. Simmons, *Phys. Rev. B*, 1990, **41**, 96.
47 V. F. Sears, *Canadian Journal of Physics*, 1966, **44**, 1279.
48 V. F. Sears, *Canadian Journal of Physics*, 1966, **44**, 1299.
49 J. A. Young and J. U. Koppel, *Phys. Rev.*, 1964, **135**, A603–A611.
50 S. Lovesey, *Theory of Neutron Scattering from Condensed Matter*, Clarendon Press, Oxford, 1984.
51 J. S. Beck, J. C. Vartuli, W. J. Roth, M. E. Leonowicz, C. T. Kresge, K. D. Schmitt, C.-W. Chu, D. H. Olson, E. W. Shappard, S. B. McCullen, J. B. Higgins and J. L. Schlenker, *J. Am. Chem. Soc.*, 1992, **114**, 10834.
52 M. Grün, I. Lauer and K. K. Unger, *Adv. Mater.*, 1997, **9**, 254.
53 *Material Matters*, 2008, **3.1**, 17.
54 S. Brunauer, P. Emmet and E. Teller, *J. Am. Chem. Soc.*, 1938, **60**, 309.
55 M. Kruk, M. Jaroniec and A. Sayari, *Langmuir*, 1997, **15**, 5410.
56 G. Ehlers, A. A. Podlesnyak, J. L. Niedziela, E. B. Iverson and P. E. Sokol, *Review of Scientific Instruments*, 2011, **82**, year.
57 T. Mason, D. Abernathy, I. Anderson, J. Anker, T. Egami, G. Ehlers, A. Ekkebus, G. Granoth, M. Hagen, K. Herwig, J. Hodges, C. Hoffman, C. Horak, L. Horton, F. Klose, J. Larese, A. Mesecar, D. Myles, J. Neuefeind, M. Ohl, C. Tulk, X. Wang and J. Zhao, *Physica B: Condensed Matter*, 2006, **385386, Part 2**, 955 – 960.
58 R. Azuah, L. Kneller, Y. Qiu, P. Tregenna-Piggott, C. Brown, J. Copley and R. Dimeo, *J. Res. Natl. Inst. Stan. Technol.*, 2009, **114**, 341.
59 K. S. W. Sing, D. H. Everett, R. A. W. Haul, L. Moscou, R. A. Pierotti, J. Rouquérol and T. Siemieniewska, *Pure Appl. Chem.*, 1985, **57**, 603.
60 K. J. Edler, P. A. Reynolds, P. J. Branton, F. R. Trouw and J. W. White, *J. Chem. Soc., Faraday Trans.*, 1997, **93**, 1667–1674.
61 F. Rouquerol, J. Rouquerol and K. Sing, *Adsorption by Powers and Porous Solids: Principles, Methodology, and Applications*, Academic Press, San Diego, 1999.
62 D. E. O'Reilly and E. M. Peterson, *J. Chem. Phys.*, 1977, **66**, 934–937.
63 P. A. Egelstaff, *An Introduction to the Liquid State*, Oxford University Press, 1994.
64 D. G. Narehood, *PhD thesis*, The Pennsylvania State University, 2003.
65 P. L. Hall and D. K. Ross, *Molecular Physics*, 1981, **32**, 673–682.
66 K. S. Singwi and A. Sjölander, *Phys. Rev.*, 1960, **119**, 863.
67 B. Coasne, F. R. Hung, R. J. M. Pellenq, F. R. Siperstein and K. E. Gubbins, *Langmuir*, 2006, **22**, 194–202.
68 J. M. Drake and J. Klafter, *Phys. Today*, 1990, **43**, 46.
69 S. Granick, *Science*, 1991, **253**, 1374.
70 G. C. Xu, S. Simmons, T. S. Mahadevan, G. W. Scherer, S. H. Garofalini and C. Pacheco, *Langmuir*, 2009, **25**, 5084.
71 H. Hoang and G. Galliero, *Phys. Rev. E*, 2012, **86**, 021202.
72 J. Zhang, B. D. Todd and K. P. Travis, *J. Chem. Phys.*, 2004, **121**, 10778.
73 J. S. Hansen, P. J. Daivis and B. D. Todd, *J. Chem. Phys.*, 2007, **126**, 133706.
74 R. Elliott and W. Hartmann, *Proc. Phys. Soc.*, 1967, **90**, 671–680.
75 M. Krusius and M. Vuorio, *Proceedings of the Fourteenth International Conference on Low Temperature Physics*, 1975.
76 P. C. H. Mitchell, A. J. Ramirez-Cuesta, S. F. Parker, J. Tomkinson and D. Thompsett, *J. Phys. Chem. B*, 2003, **107**, 6838.
77 D. White and E. N. Lassettre, *J. Chem. Phys.*, 1960, **32**, 72.
78 B. Yager, J. Nyéki, A. Casey, B. P. Cowan, C. P. Lusher, J. Saunders, D. Drung and T. Schurig, *J. Low Temp. Phys.*, 2010, **158**, 213–219.
79 C. P. Lusher, J. Nyéki, A. Casey, B. P. Cowan, J. Saunders and D. E. W. Vaughan, *J. Low Temp. Phys.*, 2004, **134**, 619.
80 D. F. Brewer, D. J. Creswell, Y. Goto, M. G. Richards, J. Rolt and A. L. Thomson, *J. Low Temp. Phys.*, 2004, **134**, 619.
81 M. Krusius and M. Vuorio, *Proceedings of the Fourteenth International Conference on Low Temperature Physics*, 1975.
82 T. Matsushita, A. Kuze, R. Kawai, M. Heida and N. Wada, *J. Low Temp. Phys.*, 2013, **171**, 657.
83 C. G. Sonwane, C. W. Jones and P. J. Ludovice, *J. Phys. Chem. B*, 2005, **109**, 23395.
84 Y. L. Sandler, *J. Phys. Chem.*, 1954, **53**, 58.
85 I. F. Silvera and M. Nielsen, *Phys. Rev. Lett.*, 1976, **37**, 1275.
86 V. Buch and J. P. Devlin, *J. Chem. Phys.*, 1993, **98**, 4195.